Research papers

Temperature state prediction for lithium-ion batteries based on improved physics informed neural networks

Yuchen Wang [a,b], Can Xiong [a,b,*], Yiming Wang [c], Po Xu [c], Changjiang Ju [a,b], Jianghao Shi [a,b], Genke Yang [a,b], Jian Chu [a,b]

[a] Ningbo Artificial Intelligence, Institute of Shanghai Jiao Tong University, Ningbo, Zhejiang, 315000, China
[b] Shanghai Jiao Tong University, Department of Automation, Shanghai, 200240, China
[c] Ginlong Technologies Co., Ltd, Ningbo, Zhejiang, 315000, China

ARTICLE INFO

ABSTRACT

Heat generation significantly influences the performance of lithium-ion batteries and also hinders the application of them. Precise prediction of battery temperature can offer feedbacks to monitor system so as to enable safe and efficient operation of batteries. However, battery temperature prediction remains extremely challenging due to the increase of irreversible heat caused by aging across the life cycle. To tackle this problem, we propose a novel framework named battery informed neural network (BINN). In this paper, we incorporate battery physical models into long short-term memory (LSTM)-based networks that is trainable in an end-to-end manner for battery temperature prediction. Multi-head attention mechanism is introduced to attend to information from longer time series. Physical parameters of the battery electrical model, heat generation model, and thermal model are automatically learnt during training. The irreversible heat changes brought on by aging is considered and represented by physical parameters. Temperature prediction for the full life cycle of lithium-ion batteries using BINN is tested under different working conditions. It is shown that BINN is interpretable and has better generalization and transferability than traditional learning-based methods.

1. Introduction

Due to the characteristic of high energy density and inexpensive price, lithium-ion batteries have been widely used in multi-scale energy storage devices [1]. The states, performance, and health of batteries are significantly impacted by the heat produced by cells during charging and discharging. In order to maintain high performance in long term, it is crucial to monitor the temperature of cells precisely [2,3]. It is also desirable by current battery manage systems (BMS) because of the growing demand of safe and intelligent thermal controls. An accurate battery temperature prediction model can improve the control performance of the model predictive control (MPC) method, which is an efficiently used thermal control method in BMS [4]. The prediction model can also be applied for model-based battery thermal fault diagnosis [5] in real-time. Since the state of charge (SOC) and state of health (SOH) are correlated with the cell temperature, the predicted temperature can also support high-precision SOC [6] and SOH estimations [7,8].

Temperature can be considered as a strong nonlinear characteristic of the lithium-ion battery. The complex electrical, thermal, and heat transfer processes result in an ununiform distribution of temperature inside the cell [9]. To analyze the thermal performance of the battery, the temperature distribution inside a lithium-ion battery is modeled in [10,11] by establishing partial differential equations (PDEs). Numerous studies that use finite element methods (FEM) [12,13] to solve PDEs achieving satisfying results. For modeling methods based on FEM, geometric, material, and electrolyte parameters must be known in advance. Although these methods are highly accurate, the computation is less suitable for real-time system. Many studies have simplified the PDEs as ordinary differential equations (ODEs) to create the lumped parameter models (LPM) [14–16]. LPM requires less parameters and can be used in real-time applications, the trade-off is to degrade the accuracy of prediction and to be more sensitive to operating conditions. In model-based methods, several internal parameters are obtained by off-line parameter identification [14] or irreversible measurements [14,17]. Different working conditions may affect the accuracy of the parameter extraction. Additionally, model-based methods frequently need the creation and modification of models in accordance with various applications, which is easy for designers but challenging for users.

For control purposes and ease of implementation, core and surface temperatures of a battery are often adopted to represent the state

---

of temperature (SOT) [18]. The core temperature of the lithium-ion battery is difficult to obtain. Paper [17,19] propose that monitoring the surface temperature of the battery can effectively reflect changes of the core temperature.

Recent researches investigate the use of deep learning techniques to predict surface temperatures of lithium-ion batteries. Deep learning is user-friendly and solves the excessive model dependency in existing model-driven methods. Panchal et al. construct a feedforward neural network (FNN) model that selects discharge capacity, current, and ambient temperature as inputs to forecast cell temperatures [20]. Farzad Jaliliantabar et al. train FNN model to infer the cell temperature using discharge rate, phase change material (PCM) with and without paraffin/graphene, thickness of PCM, and time [21]. However, the temperature prediction of cells is performed with few charge and discharge cycles. Because of aging, the cell temperature rise in later life cycles will be faster under the same operating condition. Since FNN only utilizes temporary information, it is less effective and accurate in full life cycle temperature prediction. Long short-term memory (LSTM) [22] which is firstly proposed for the gradient vanishing problem of recurrent neural network (RNN), is now considered as a powerful network structure for time-domain signal prediction. In [23], the average temperature in each cycle is used as training data to predict temperature changes caused by the increased irreversible heat in later life cycles. The increase of irreversible heat at the end of battery life cycle is predicted based on learning-based method, but the lack of mechanistic modeling results in limited mobility. In addition, training and testing data sets of the same battery are applied in most experiments [20,21,23,24]. Existing learning-based methods are proved faster than FEM and more accurate than LPM, but most of them do not require explicit physical models. Due to the lack of transparency, their reliability is obscure. Meanwhile, they require enormous data to avoid overfitting, and their performance tends to deteriorate severely because of features not contained in training data. Besides, few studies have considered the aging factor when predicting long-term or full life cycle cell temperatures.

Physics informed neural network (PINN) [25] is a scientific machine learning method in numerical computation, designed especially for solving various problems related to PDEs [26,27]. The main idea of PINN is to add the residual of physical equations to the loss function in neural networks. To ensure that the trained model complies with the physical laws according to pre-defined constraints, the neural network minimizes both the residual of physical equations and the loss function of observed data during training. It is known as a hybrid model-data-driven approach with improved interpretability [28]. When solving inverse problems with uncertain parameters, it is more reliable and efficient than conventional model-based approaches [27].

Inspired by PINN, we propose a novel interpretable framework named battery informed neural network (BINN) for the temperature prediction of lithium-ion batteries in full life cycles. Coefficients of the function demonstrating the relationship between the measurement and aging, along with other physical quantities, are established as under determined parameters learned by BINN. The selected features (voltage, current, experiment time, etc.) together with hidden states of the previous output are fed to BINN to obtain the current output (cell surface temperature, open circuit voltage). The rest of the paper is organized as follows, Section 2 presents physical models of the battery that embedded in BINN. Section 3 illustrates the architecture of BINN. Section 4 gives the details of experiment. Section 5 compares the experiment results of conventional learning-based methods, PINN, and BINN in prediction performance. A conclusion is included in Section 6.

2. Physical models of lithium-ion batteries for temperature state prediction

Since the coupling of electric, thermal, and heat transfer are main contributors to cell temperatures, the battery temperature variation can be inferred by combining the electrical model, heat generation model, and battery temperature model.

2.1. The electrical model of lithium-ion batteries

Equivalent circuit model and pseudo-two-dimensions (P2D) model are two classical models that describe the electrochemical characteristics of lithium-ion batteries. Compared with P2D model, the equivalent circuit model is simple yet as effective in the task of predicting temperatures [16], and does not require additional measurements during regular battery charging and discharging. The most commonly used equivalent circuit models are R_{int} model, Thevenin model, and partnership for a new generation of vehicles (PNGV) model. The above equivalent circuit models which represent different complexity are embedded in our proposed framework for experiments. The following section will demonstrate the detail of framework and explain how to embed the given physical model. The results show that the framework with different electrical model embedded can accurately predict the temperature when the training of neural networks converges. However, complex electrical models make the parameter optimization process of neural networks more difficult and need more training time. In this study, the R_{int} model is adopted accounting for training time and accuracy. The introduction to the equivalent circuit models mentioned above as well as the results of the experiment can be found in Appendix.

The calculation of the R_{int} model is listed in (1), where U_{ocv} is the open-circuit voltage, R_0 is the internal resistance, I is the current and U_t is the cell voltage.

$$U_t = U_{ocv} - I * R_0 \tag{1}$$

2.2. The heat generation model of lithium-ion batteries

Thomas and Newman [29] derived Eq. (2) for the heat generation of a lithium-ion battery based on experiments.

$$q = I(U_{ocv} - U_t) - IT_{in}\frac{\partial U_{ocv}}{\partial T_{in}} - \sum_i \Delta H_i^{avg} r_i - \int \sum_j (\overline{H_j} - \overline{H_j^{avg}})\frac{\partial c_j}{\partial t}\, dv \tag{2}$$

q is defined as the rate of heat generated or consumed, I is the current (positive when charge), T_{in} is the core temperature of the battery, $\frac{\partial U_{ocv}}{\partial T_{in}}$ is the entropic coefficient, the enthalpy variation of a chemical reaction i is defined as ΔH_i, r_i is the rate of chemical reaction i, $\overline{H_j}$ stands for the partial molar enthalpy of species j, c_j represents concentration, t is time, and v is the volume. The properties are measured at the volume-averaged concentration, as shown by the superscript "avg". The irreversible heat produced by the internal resistance dissipation is described in the first term of Eq. (2). The second term is the reversible entropic heat which is related to cell reactions. The third term denotes the heat generated or absorbed by any potential chemical reactions that might take place in the cell. Since the side effects accounting for aging often occur slowly, it is negligible. The last term accounts for the heat of mixing, which is produced by the development and relaxation of concentration gradients inside the cell. Concentration gradients are constrained in electrochemical systems of good transport properties, therefore it is also negligible.

2.3. The thermal model of lithium-ion batteries

In [17], Christophe Forgez et al. develop a lumped-parameter thermal model for cylindrical LiFePO$_4$/graphite lithium-ion batteries shown in Fig. 1.

The model applies heat source, heat capacity, and thermal resistance to simulate the heat generation and dissipation of a cell. The surface temperature is obtained according to energy balance given in (3).

$$\frac{dT_s}{dt} = \frac{T_{amb} - T_s}{C_p(R_{in} + R_{out})} + \frac{qR_{out}}{C_p(R_{in} + R_{out})}$$
$$\frac{R_{in}}{R_{out}} = \frac{T_{in} - T_s}{T_s - T_{amb}} \tag{3}$$
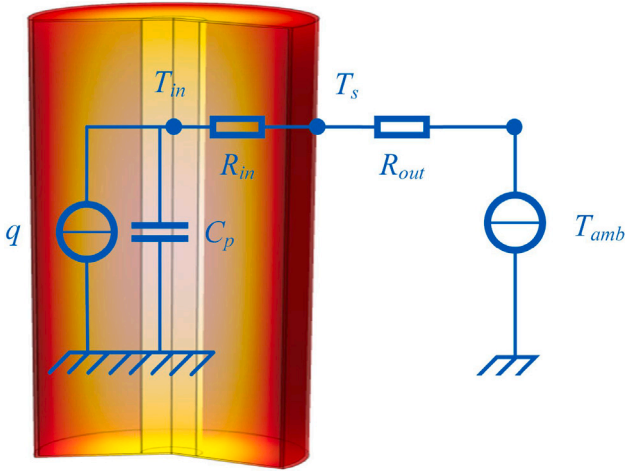
Fig. 1. The circuit in the thermal model.

C_p is the heat capacity, T_{in} is the internal temperature of the cell, T_s is the surface temperature of the cell, R_{in} is heat transfer resistance inside the cell, R_{out} is heat transfer resistance outside the cell, and T_{amb} is the ambient temperature. The essential factors of the heat generation model are provided by the battery electrical model. Heat production and heat transfer in the thermal model result in the temperature increase. In this research, the electric, thermal, and heat transfer processes form the full battery physics model, enabling exact tracing from heat creation to temperature variation.

In this study, the characteristics include observed information of the battery surface temperature, time information, and aging are selected as the input features $x(t)$ for BINN, given in (4).

$$x(t) = [t, U_t, I, \text{SOC}, T_{amb}, C_{last}, N_{cycle}]^\tau \in \mathbb{R}^6 \times \mathbb{N} \tag{4}$$

The output $y(t)$ of BINN is defined as (5).

$$y(t) = [T_s, U_{ocv}]^\tau \in \mathbb{R}^2 \tag{5}$$

where,

t : the experiment time.
U_t : voltage of the cell.
I : current of the cell.
SOC : the cell state of charge.
T_{amb} : the ambient temperature.
C_{last} : the maximum discharge capacity of the last cycle.
N_{cycle} : the number of cycles.
T_s : the cell surface temperature.
U_{ocv} : the open circuit voltage of the cell.

3. Methodology of BINN

A traditional hybrid model-data-driven approach [30] is processed with the feature engineering as the first step, namely, feeding observable data into the determined physical model shown by Fig. 2(a). The original input is passed through the physical model with prior information to obtain higher dimensional information, which contains important hidden features. It is then fed into the neural networks together with the model output. According to existing prior information, the appropriate network structure can be determined. For instance, FNN is commonly chosen for regression and classification, RNN or LSTM may be chosen for time series prediction. The network weights are optimized by minimizing the difference between labels and predicted values through supervised learning, but the learning procedure cannot guarantee the solution to be global optimal that approximates practical conditions under the selected network structure. In fact, the connection between model and data in traditional model-data-driven methods is mainly established by feature engineering.

Except for feature engineering, PINN provides soft constraints by adding residuals of physical equations and initial and boundary conditions to the loss function. The converged neural network is considered as the most proper solution satisfying the physical laws as shown in Fig. 2(b). Undetermined parameters of the physical model can be set as learning parameters in the neural network during optimizations.

3.1. General description of BINN

Consider the problem of predicting a nonlinear dynamic system state $s(t_n)$, described by (6).

$$s(t_n) = f(s(t_{n-1}), u(t_n); \theta) \tag{6}$$

The current state $s(t_n)$ is determined by the previous state $s(t_{n-1})$ and the current external driving signal $u(t_n)$. Since obtaining the system state under test conditions is challenging, FNN applied in PINN is replaced by LSTM in BINN because of its closed-loop network structure to tackle the problem. The model of BINN is provided in (7),

$$y(t_n) = BINN(x(t_n), h(y(t_{n-1})); \theta, \lambda) \tag{7}$$

where $y(t_n) = [y_1(t_n), y_2(t_n), \ldots, y_m(t_n)]^\tau$ is the output at n moment, $x(t_n) = [x_1(t_n), x_2(t_n), \ldots, x_p(t_n)]^\tau$ represents the input feature that incorporates certain system states and external driving signals defined on domain $\Omega \subset \mathbb{R}^p$, and $h(y(t_{n-1}))$ is the hidden state of the latest output. Both $x(t_n)$ and $h(y(t_{n-1}))$ are utilized as input in BINN. θ is a neural network parameter and λ is the unknown parameter in the physical model.

Suppose that the physical system satisfies differential equations given in (8) and boundary conditions shown in (9) at moment t_n. Time t is taken into account as a component of $x(t_n)$, the initial condition can be regarded as a special boundary condition for the spatio-temporal domain.

$$f\left(x(t_n); \frac{\partial y_k}{\partial x_i}; \frac{\partial^2 y_k}{\partial x_i \partial x_j}; \ldots; \lambda\right) = 0, \ x(t_n) \in \Omega \tag{8}$$
$$(i = 1, \ldots, p, j = 1, \ldots, p, k = 1, \ldots, m)$$

$$B(y(t_n), x(t_n)) = 0, \quad on \quad \partial\Omega \tag{9}$$

To encode the physical requirements into the neural network, the loss function can be divided into three parts, as demonstrated in (10).

$$L(\theta, \lambda; D) = w_f L_f(\theta, \lambda; D_f) + w_b L_b(\theta, \lambda; D_b) + w_u L_u(\theta, \lambda; D_u) \tag{10}$$

L_f is the residual of differential equations, and L_b is the residual of boundary conditions. To obtain the unknown parameters λ in the physical model, additional data of observations satisfying $U(y(t_n), x(t_n)) = 0$ are required. L_u is the residual of the introduced observations. w_f, w_b, and w_u is the weight of each term, respectively.

$$L_f(\theta, \lambda, D_f) = \frac{1}{|D_f|} \sum_{x(t_n) \in D_f} \left| f\left(x(t_n); \frac{\partial y_k}{\partial x_i}; \frac{\partial^2 y_k}{\partial x_i \partial x_j}; \ldots; \lambda\right) \right|^2$$
$$(i = 1, \ldots, p, j = 1, \ldots, p, k = 1, \ldots, m)$$
$$L_b(\theta, \lambda, D_b) = \frac{1}{|D_b|} \sum_{x(t_n) \in D_b} \left| B(y(t_n), x(t_n)) \right|^2 \tag{11}$$
$$L_u(\theta, \lambda, D_u) = \frac{1}{|D_u|} \sum_{x(t_n) \in D_u} \left| U(y(t_n), x(t_n)) \right|^2$$

The calculation of each term is listed in (11). The training data are constructed as $D = \{x(t_1), x(t_2), \ldots, x(t_{|D|})\}$, where $|D|$ is the size. D is divided into three sets, D_f, D_b, and D_u. D_f and D_u correspond to sets inside the domain, D_b corresponds to the set on the boundary. The network training is to optimize θ and λ simultaneously, the solution is $\theta^*, \lambda^* = argmin_{\theta, \lambda} L(\theta, \lambda; D)$
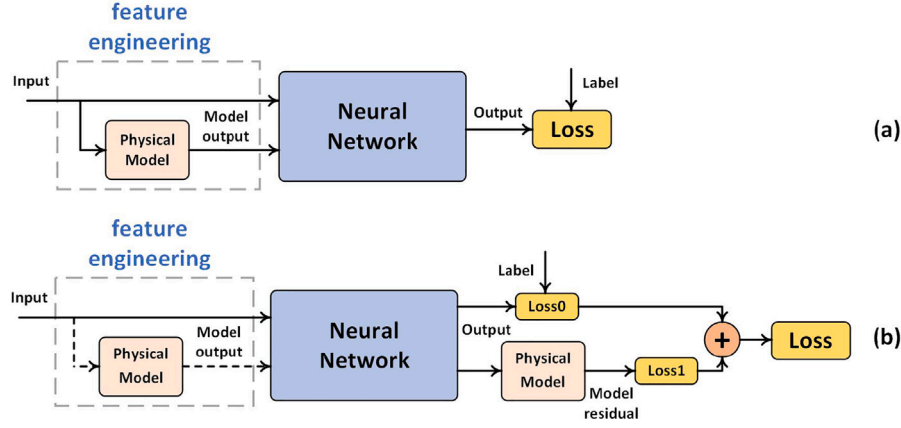
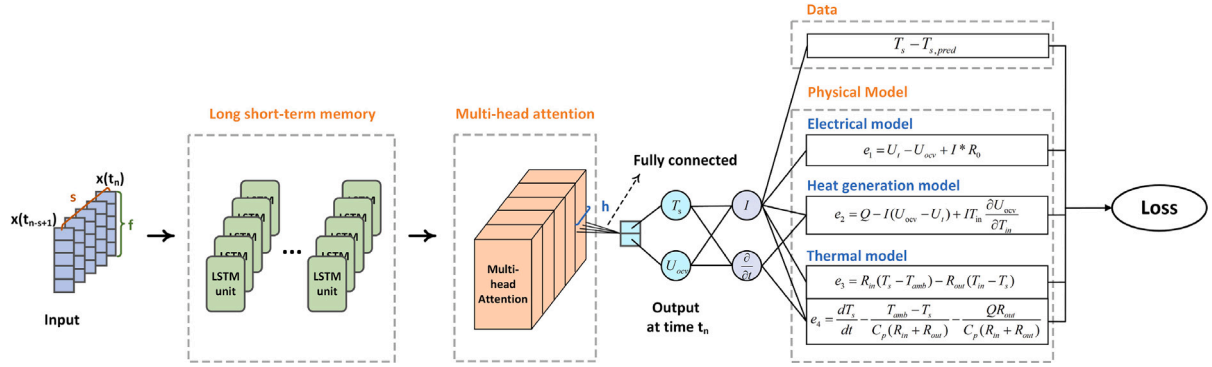**Fig. 2.** (a) traditional hybrid model-data-driven approach; (b) PINN approach.

Fig. 3. Structure of BINN.

3.2. Implementation of BINN for battery temperature prediction

On the task of cell temperature prediction, the structure of BINN is shown in Fig. 3. The initial conditions are not specified, which makes it flexible for inference by the trained model. The coupled electric-heat and heat transfer model of the battery is used as a soft constraint, and the cell temperature data of full life cycles are used as additional data to determine unknown model parameters, so that a battery thermal model that conforms to training data can be obtained.

BINN takes the form of sliding windows to make predictions. The input x_{in} and the output y_{out} of BINN is defined as (12).

$$x_{in} = [x(t_{n-s+1}), \ldots, x(t_n)]^\tau$$
$$y_{out} = [y(t_n)] \tag{12}$$

Wherein $x(t_n)$ is referred to (4), s is the number of timesteps feeding into BINN. $y(t_n)$ is the output at the t_n sampling moment refer to (5). According to [31], the open circuit voltage depends on both the input characteristics and the cell surface temperature which is another output information, shown by (13).

$$U_{ocv} = f(SOC, T_s) \tag{13}$$

When predicting the output at the current moment t_n, BINN requires input $x(t_n)$ together with the hidden state of the previous output.

Since the temperature of a cell changes slowly, the heat generated by the electrochemical reaction takes time to be conducted to the surface of the cell. Accurately predicting the current temperature of the cell via LSTM needs information from long time steps in history. Therefore, for long time series, the memory of LSTM is very limited. The attention mechanism is introduced to capture long-sequence dependencies and aggregate information, which addresses the issue of limited

LSTM memory units. Thus, the accuracy of inference prediction can be greatly improved.

The loss function in BINN is shown in (14), where w_p is the weight of data loss and w_{e_i} represents the individual loss weight of the physical model.

$$L(\theta, \lambda) = L_p(\theta, \lambda) + L_e(\theta, \lambda)$$
$$L_p(\theta, \lambda) = w_p \frac{1}{N} \sum_{n=1}^{N} \left| T_s^n - T_{s,pred}^n \right|^2 \tag{14}$$
$$L_e(\theta, \lambda) = \sum_{i=1}^{4} w_{e_i} \frac{1}{M} \sum_{n=1}^{M} |e_i^n|^2$$

In the forward pass, the input goes through n layers of LSTM to obtain hidden states. The multi-head attention layer projects hidden states into h linear space to perform information decoding and weighting for long timesteps sequential input. The two-dimensional output tensor is obtained through full connections. The surface temperature of the cell is used as the observed data to optimize network parameters θ and λ. The physical battery model is encoded into the network structure by adding the residuals of the physical equations to the loss function. The derivation of the output with respect to the input is achieved by automatic differentiation (AD) to satisfy the physical requirements. In the back-propagation, Adam optimizer is applied to minimize the total loss.

LSTM is a special RNN that can retain more information through three gates inside: an input gate, an output gate, and a forget gate. The LSTM unit accepts the output value of the previous moment $h(y(t_{n-1}))$ along with the input value of the current moment $x(t_n)$ as the complete input. The input gate i_n controls input values flowing into the LSTM unit, the forget gate f_n selects the value of the last LSTM unit state u_{n-1} that will be preserved, and the output gate o_n figures out which values

are adopted to compute the final output $h(y(t_n))$. $\widetilde{u}_n$ is the transformed input which is controlled by input gate i_n. u_n is the current state that contains the memory of previous units. The activation function of LSTM gates are the "sigmoid(σ)" function and "tanh" function.

$$
\begin{aligned}
i_n &= \sigma(W_i * [h(y(t_{n-1})), x(t_n)] + b_i) \\
f_n &= \sigma(W_f * [h(y(t_{n-1})), x(t_n)] + b_f) \\
o_n &= \sigma(W_o * [h(y(t_{n-1})), x(t_n)] + b_o) \\
\widetilde{u}_n &= \tanh(W_u * [h(y(t_{n-1})), x(t_n)] + b_u) \\
u_n &= \sigma(f_t * u_{n-1} + i_n * \widetilde{u}_n) \\
h_n &= \tanh(u_n) * o_n
\end{aligned}
\tag{15}
$$

The calculations in a LSTM unit are listed in (15). Although the LSTM structure is capable of memorizing historical data, information contained in earlier time steps may be lost for lengthy inputs because LSTM computes sequentially.

Multi-head attention mechanism is proposed as the core module in Transformer [32]. Compared with the traditional self-attention mechanism, multi-head attention projects inputs into different linear spaces through different transformation matrices W_i^Q, W_i^K, and W_i^V ($i = 1,2...h$). It helps the network to capture richer features. Due to reduced dimensions of each head, the total computational complexity will not be evidently increased compared with the single-head attention mechanism.

Eq. (16) illustrates the process of multi-head attention mechanism.

$$
Q_i = xW_i^Q, K_i = xW_i^K, V_i = xW_i^V \ (i = 1, 2 \ldots h)
$$
$$
\text{MultiHead}(Q, K, V) = \text{Concat}(\text{head}_1, \ldots, \text{head}_h)W^O
\tag{16}
$$
$$
\text{head}_i = \text{Attention}(Q_i, K_i, V_i)
$$

where $W_i^Q \in \mathbb{R}^{d_{in} \times d_k}$, $W_i^K \in \mathbb{R}^{d_{in} \times d_k}$, $W_i^V \in \mathbb{R}^{d_{in} \times d_v}$, $W^O \in \mathbb{R}^{hd_v \times d_{in}}$, d_{in} is the dimension of the input, d_k is the dimension of queries and keys, d_v is the dimension of values, and h is the number of headers. Multi-head self-attention allows models to learn independently through different sets of linear projections W_i^Q, W_i^K, and W_i^V ($i = 1,2...$, h) to transform input to queries Q_i, keys K_i, and values V_i, respectively. h attention output can be obtained through scaled dot-product attention using transformed Q_i, K_i, V_i. Then, h attention outputs are concatenated together and transformed by another linear projection W^O which is learned to produce the final output.

$$
\text{Attention}(Q_i, K_i, V_i) = \text{softmax}\left(\frac{Q_i K_i^{\tau}}{\sqrt{d_k}}\right)V_i
\tag{17}
$$

The formula of the scaled dot-product attention is shown in (17). After computing the dot product of each query and all keys divided by $\sqrt{d_k}$, a softmax function is applied to obtain the attention score. Finally, the attention output head_i is derived by multiplying the values.

3.3. Prior information of aging via internal resistance

Unlike computational methods, in BINN there is no guarantee of unique solutions, because solutions are obtained by solving nonconvex optimization problems [28]. Prior information of the cell is considered to achieve a nearly global optimal solution. Internal resistance is a key parameter that BINN relies on to achieve full life cycle temperature prediction. The internal resistance determines the amount of irreversible heat in the battery heat generation model. In the electrical model, changes in the electrical characteristics of the battery affect the magnitude of the resistance during a single charging and discharging process. Anosh Mevawalla [16] established the relationship among internal resistance, current, and SOC in the R_{int} model for charging and discharging process without considering aging (18).

$$
R_{\text{int}} = \left(A_1 + A_2 \frac{\ln\left(\frac{I}{A_3} + \sqrt{\frac{I^2}{A_3^2} + 1}\right)}{I} \right) e^{A_4 \text{SOC}}
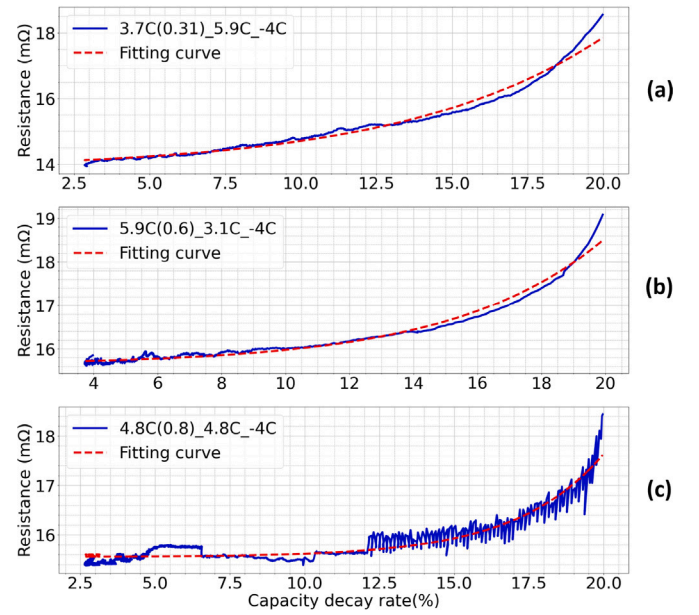\tag{18}
$$

Fig. 4. (a) (b) (c) shows the resistance measured under three fast charge conditions and the fitting curve of (19). "$3.7C(0.31)\_5.9C\_-4C$" means charging with 3.7 C up to 31% SOC then charging with 5.9 C till reaching the rated voltage. The battery finally charges with constant voltage and discharges at 4 C.

The aging of the battery can be characterized by the change of internal resistance. It is necessary to consider the rising irreversible heat caused by the increment of internal resistance during operation. To add aging factor to (18) and further represent the internal resistance, the dataset, made up of 124 commercial lithium-ion batteries that were fast-charged under various settings until they failed, is analyzed [dataset] [33]. Internal resistance measurements were obtained during charging at 80% SOC by averaging 10 pulses of ±3.6 C with a pulse width of 30 ms (2017-05-12 and 2017-06-30) or 33 ms (2018-04-12). It can be observed that the variation trend of internal resistance under all operating conditions can be well fitted by exponential function. Fig. 4 shows the relationship between internal resistance and capacity decay rate under different operation conditions and the results of exponential function fitting. The calculation of capacity decay rate δ_{decay} and the fitting function is show in (19). C_{cycle} is the current capacity and C_{max} is the rated capacity. In this paper, the value of C_{cycle} is taken as maximum discharge capacity of the last cycle C_{last}, since the aging of battery between adjacent cycles is negligible. Root mean square error (RMSE) is used to evaluate the performance of fitting. Table 1 lists the fitting results and RMSE under different conditions.

$$
\delta_{decay} = 1 - \frac{C_{cycle}}{C_{\max}}
\tag{19}
$$
$$
R = B_1 e^{B_2 \delta_{decay}} + B_3
$$

Finally, (20) is used to represent the internal resistance in BINN. The first term represents variation of the internal resistance in a cycle. The second term indicates the increasing trend of the internal resistance caused by aging. Although temperature does not appear explicitly in the expression of internal resistance, the electrical model, the heat generation model, and the thermal model are satisfied simultaneously. In the electrical model, the value of internal resistance is related to the open circuit voltage. As the output, the open circuit voltage is temperature dependent satisfying all of the three models. Wherein the parameters A_1, A_2, A_3, B_1, B_2 can be regarded as the undetermined parameter in the inverse problem, which is set as the parameter of the network and learned by optimizing the loss function. When BINN predicts the value of internal resistance, it actually considers the effect
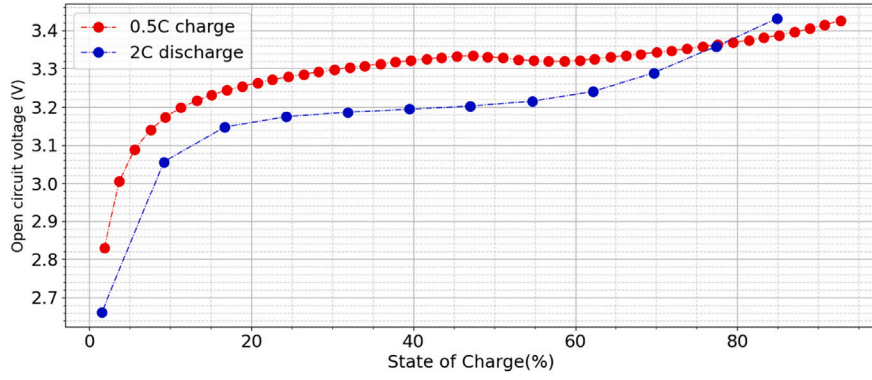
Fig. 5. The open circuit voltage changes of lithium-ion battery on the test set.

Table 1
Variation trend of internal resistance under different conditions.

Condition	$B1$	$B2$	$B3$	RMSE
$3.7C(0.31)\_5.9C\_-4C$[a]	1.94e−4	15.17	1.38e−2	1.00e−4
$5.9C(0.6)\_3.1C\_-4C$	4.13e−5	21.28	1.56e−2	6.38e−5
$4.8C(0.8)\_4.8C\_-4C$	2.24e−6	34.18	1.55e−2	1.35e−4
$5C(0.67)\_4C\_-4C$	3.63e−6	32.24	1.52e−2	4.21e−5
$6C(0.2)\_4.5C\_-4C$	2.00e−3	5.36	1.54e−2	1.89e−4
$4.9C(0.27)\_4.75C\_-4C$	4.70e−3	2.78	1.21e−2	1.34e−4
$4C(0.04)\_4.85C\_-4C$	3.40e−3	3.41	1.33e−2	1.11e−4
$8C(0.35)\_3.6C\_-4C$	4.63e−4	10.68	1.63e−2	2.15e−4

[a] "$3.7C(0.31)\_5.9C\_-4C$" means charging with 3.7 C up to 31% SOC then charging with 5.9 C till reaching the rated voltage. The battery finally charges with constant voltage and discharges at 4 C.

Table 2
The parameters of (3) and (20).

Parameters	0.5 C charging and 2C discharging at 35 °C
R_{in} (k W^{-1})	3.305
R_{out} (k W^{-1})	8.903
C_p (J K^{-1})	74.901
A_1	7.887e−4
A_2	7.983e−2
A_3	6.844
A_4	−0.120
B_1	5.947e−4
B_2	24.979

of temperature.

$$R_0 = \left(A_1 + A_2 \frac{\ln\left(\frac{I}{A_3} + \sqrt{\frac{I^2}{A_3} + 1}\right)}{I} \right) e^{A_4 \text{SOC}} + B_1 e^{B_2 \delta_{decay}} \tag{20}$$

4. Experimental setup

BINN is evaluated on a data set provided by Sandia National Laboratories in the United States [dataset] [34], which contains full life cycle data of LiFePO$_4$ (LFP), LiNi$_x$Co$_y$Al$_{1-x-y}$O$_2$ (NCA), and LiNi$_x$Mn$_y$Co$_{1-x-y}$O$_2$ (NMC) batteries that operate under different ambient temperatures, depths of discharge, and discharge currents until the capacity decays to 80%. For experiments, the typical operating data of the LFP battery (Part #APR18650M1 A, 1.1 Ah) under various ambient temperature is used.

$$\text{SOC(t)} = \text{SOC}_0 - \frac{\int_0^t I(t)dt}{C_{cycle}^{\max}} \tag{21}$$

The original data set contains experimental cycles and time, the charge and discharge capacity and energy, the terminal voltage, the current and the ambient temperature. Using the initial value of SOC_0 in each cycle and the maximum charge and discharge capacity $C_{cycle}^{\max}$, the SOC is calculated according to the ampere hour integration method (21). A positive discharge current and a negative charge current are defined in (21).

The maximum discharge capacity of the last cycle is added as a feature to enable the neural network to learn the effects of aging. The normalized experimental time, voltage, current, SOC, ambient temperature, cycle times, and maximum discharge capacity of last cycle are selected as the input of the neural network.

The neural networks are trained on an NVIDIA RTX3090 GPU. In this experiment, the initial learning rate for training is set to 0.0001. The hyperparameters w_p and w_{e_i} are recommended to be tuned during the training process. User can adjust these parameters to facilitate that each term in the loss function is on the same order of magnitude, thereby accelerating the training process. In this study, the values of w_p and w_{e_i} were set to 1, 10, 100, 100 and 100 respectively, when the neural networks converged. The body of the network adopts 3-layer LSTMs with 200 neural units in each layer. In multi-head attention layer, the dimension of d_k and d_v is 200, and the number of heads h is taken 8. In most working conditions, the timesteps s is 40. After convergence of the training, the each inference time of BINN is 0.74 s on an 11th Gen Intel(R) Core(TM) i9-11900K @ 3.50 GHz 3.50 GHz CPU device, indicating that BINN is well-suited for real-time applications.

5. Results and discussion

5.1. Physical model parameters learned by BINN

By unsupervised optimization of residuals of the battery physical model through the network training, the predicted temperature as well as some of the battery physical model parameters, such as open circuit voltage, internal resistance, entropy coefficient, heat capacity, and thermal resistance, can be obtained when the network converges. Wherein the open circuit voltage is the output quantities varying with the input. Thermal capacitance and thermal resistance are constants that best match the physical model and training data. Internal resistance is a function identified from the training data related to the input. In the following experiment, the training set consists of the full life cycle data of one LFP battery under 0.5 C charging and 2 C discharging operation at 35 °C ambient temperature. The other LFP battery operating under the same conditions is selected as the test set.

The parameters in (3) and (20) learned through the network are shown in Table 2. The relationship between the open circuit voltage and SOC of the charging and discharging process in the test set is shown in Fig. 5. The open circuit voltage rises along with the SOC during the charging and discharging of the cell. It is worth noting that the open-circuit voltage value learned by BINN maybe varied from the open-circuit voltage value of the battery measured by real experiments. This gap depends on the accuracy of the input data and the selected circuit model, hence it is not discussed in this article in detail.
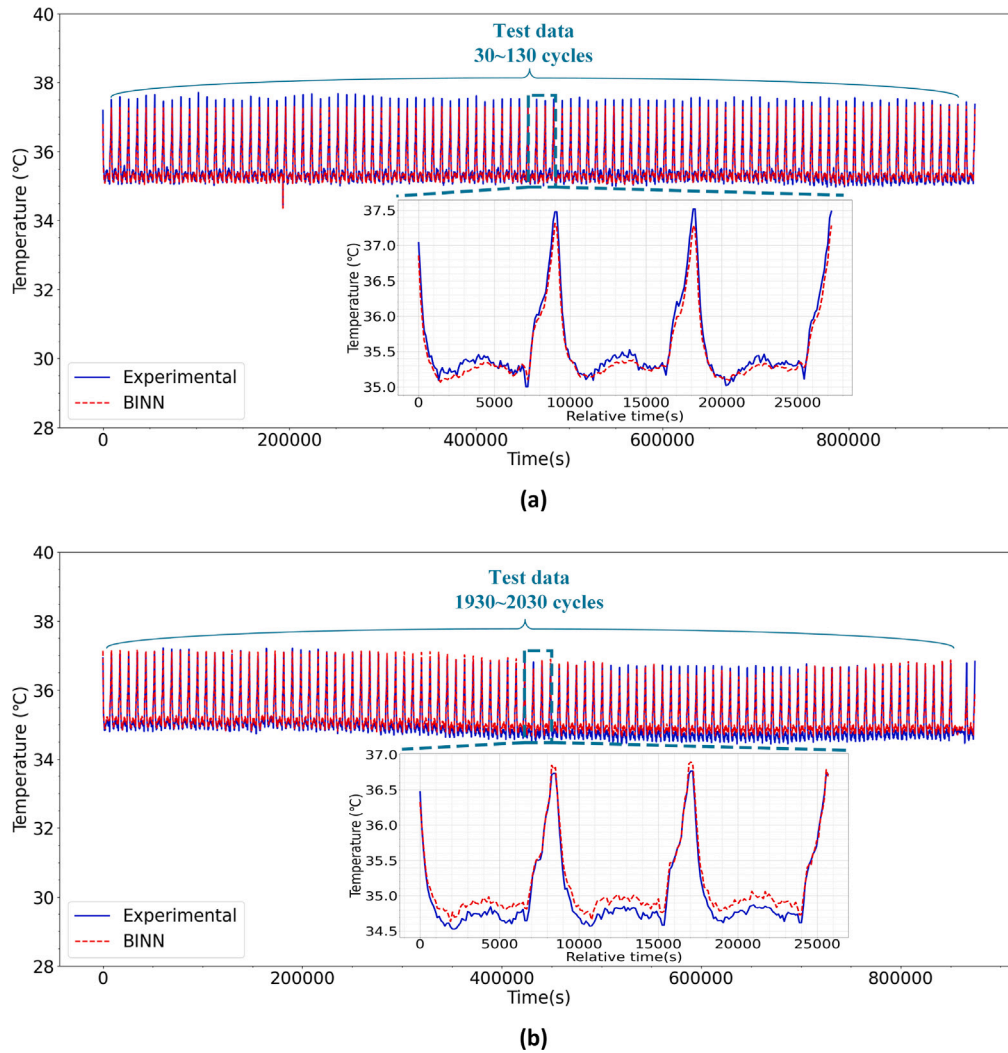
Fig. 6. Full life cycle temperature prediction of LFP battery under 0.5 C charging and 2 C discharging conditions at 35 °C ambient temperature.

Table 3
MSE of different methods under various conditions.

Condition	FNN	LSTM	PINN	BINN
LFP battery 0.5 C charge 2 C discharge at 35 °C	0.243	0.141	0.123	**0.048**
LFP battery 0.5 C charge 3 C discharge at 25 °C	0.203	0.202	0.267	**0.137**
LFP battery 0.5 C charge 1 C discharge at 15 °C	0.348	0.282	0.351	**0.150**

5.2. Temperature prediction of lithium-ion battery

To demonstrate the temperature prediction performance of the full life cycle, a training set is created using the full life cycle data of an LFP battery charged at 0.5 C and discharged at 2 C at ambient temperature of 35 °C. The trained model forecasts the life cycle surface temperature of another LFP battery under identical conditions. Fig. 6 displays prediction results of BINN on the 30th to 130th cycles and 1930th to 2030th cycles of the test set for exhibition purposes. It is noteworthy that the data set provided by Sandia National Laboratories does not include the full life internal temperature of the battery. Thus, the internal temperature obtain by BINN is a feasible solution according to the developed physical model (3) and the parameters of neural networks. We believe that if the internal temperature data is incorporated, the internal temperature prediction will be more robust.

BINN has improved generalization compared with data-driven methods. The generalization capability is illustrated by two cases. The first case is that the operation conditions of the cell in the test set falls into the distribution of training data. The following experiments are tested on different batteries under the same operating conditions as the training data. The test set for the experiment is chosen randomly from a set of lithium-ion battery data with common ambient conditions (15 °C–35 °C) and typical discharge rates (1 C–3 C).

The mean square error (MSE) of predicted values and experimental measurements is applied to evaluate the prediction accuracy shown in Table 3. For comparison, FNN, LSTM, and PINN, and BINN are set the same with 200 neurons of 3 layers. (PINN uses feedforward neural networks). The results show that BINN gives more accurate predictions, compared with the existing methods.

The second case is that the battery working condition of the test set is outside the distribution of the training set data. The prediction accuracy of all methods deteriorate. Therefore, BINN outperforms other data-driven methods in this case. The following comparison experiments are conducted between BINN and LSTM, and tested on different batteries under the different operating conditions as the training data. During the training process, the data of 0.5 C charging and 2 C discharging at 25 °C ambient temperature are used. Another set of data of 0.5 C charging and 3 C discharging at the same ambient temperature is taken as the test set. Fig. 7(a) shows the prediction performance of BINN, and Fig. 7(b) shows the prediction performance of LSTM. Since the training data is with 2 C discharge, LSTM predicts a lower temperature under the condition of 3 C discharge, while BINN shows
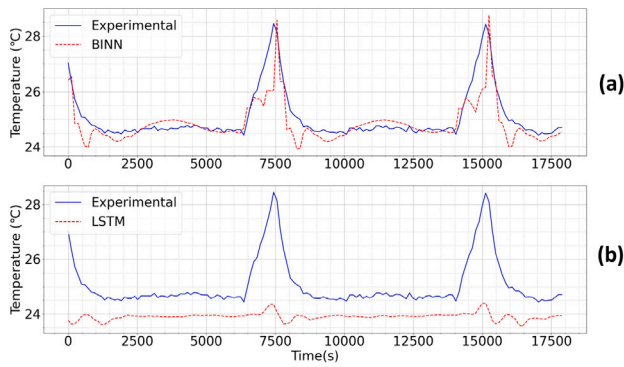
Fig. 7. (a) temperature prediction of pretrained BINN test on the 0.5 C charging and 3 C discharging condition; (b) temperature prediction of pretrained LSTM test on the 0.5 C charging and 3 C discharging condition.

better prediction results. The MSE of the two on the test set are 1.076 and 2.780, respectively.

In practice, new data will be used for incremental training as the real-world working environment changes. BINN still occupies good migration performance. When switching to a completely different working condition that is absent from the prior training set, the pre-trained BINN only requires a small amount of data under the new operating conditions for incremental training and can predict the temperature accurately. The experiment is conducted as followings, BINN and LSTM are pre-trained using the full life cycle data of 0.5 C charging and 3 C discharging at 25 °C. To predict the cell temperature with 0.5 C charging and 1 C discharging condition at the ambient temperature of 35 °C, both models use 0 to 30 cycles of a new cell data for incremental training. Fig. 8(a), (b) shows the 30 to 230 cycles prediction results of BINN and LSTM. Their MSEs are 0.026 and 15.021, respectively. It can be seen that LSTM has a good prediction in the later cycle within a small interval shown in Fig. 8(c), but the subsequent prediction precision is greatly reduced shown in Fig. 8(d). It is due to overfitting caused by inadequate data. BINN has consistently maintained a good prediction performance in the long-term prediction, since it is provided with a nearly optimal solution satisfying the real-world physical system.

6. Conclusion

In this paper, we propose a novel learning-based framework with physical models of lithium-ion batteries, realizing the full life cycle temperature prediction of cells. The method named BINN is a hybrid model-data-driven approach with improved interpretability which can not only predict the temperature of lithium-ion batteries, but also infer physical quantities that are difficult to measure, such as heat capacity, thermal resistance, open circuit voltage, and internal resistance. The increasing of internal resistance because of aging can be learned by BINN. Precise temperature prediction for the full life cycle is achieved under different working conditions. Compared with other data-driven methods, BINN has strong transferability and generalization due to the deeply embedded physical models. This research can be beneficial for early warning of thermal abuse and improving the performance of battery thermal control. The proposed method can also be utilized to forecast other states of lithium-ion batteries, including SOC, SOH, etc. Our future work will explore the application of BINN in SOC, SOH predictions.

CRediT authorship contribution statement

Yuchen Wang: Conceptualization, Methodology, Software, Validation, Writing – original draft. **Can Xiong:** Conceptualization, Investigation, Writing – review & editing. **Yiming Wang:** Data curation,

Investigation, Resources. **Po Xu:** Visualization, Project administration, Supervision. **Changjiang Ju:** Methodology, Writing – review & editing, Funding acquisition. **Jianghao Shi:** Formal analysis, Data curation, Visualization. **Genke Yang:** Supervision, Writing – review & editing. **Jian Chu:** Supervision, Project administration.

Declaration of competing interest

The authors declare the following financial interests/personal relationships which may be considered as potential competing interests: Yuchen Wang, Can Xiong, Changjiang Ju, Jianghao Shi, Genke Yang, Jian Chu reports financial support was provided by China National R&D Key Research Program. Yiming Wang, Po Xu reports financial support was provided by Ginlong Technologies Co.,Ltd.

Data availability

The authors do not have permission to share data.

Appendix. Supplement experiment

The circuit used in the R_{int} model is shown in Fig. A.1. The electrical properties can be represented by (A.1), where U_{ocv} is the open-circuit voltage, R_0 is the internal resistance, I is the current and U_t is the cell voltage.

$$U_t = U_{ocv} - I * R_0 \tag{A.1}$$

The circuit used in the Thevenin model is shown in Fig. A.2. The electrical properties can be represented by (A.2), where R_0 is the ohmic internal resistance, R_p the polarization internal resistance, C_p is the polarization capacitance and U_p is the voltage on C_p.

$$U_t = U_{ocv} - I * R_0 - U_p$$
$$\frac{dU_p}{dt} = -\frac{U_p}{R_p C_p} + \frac{I}{C_p} \tag{A.2}$$

The circuit used in the PNGV model is shown in Fig. A.3. The electrical properties can be represented by (A.3), where C_b is the energy

Table A.1
MSE of temperature prediction with different electrical models embedded in BINN.

Condition	R_{int} [a]	Thevenin	PNGV
LFP battery 0.5 C charge 2 C discharge at 35 °C	0.0602	0.0662	0.0616
LFP battery 0.5 C charge 3 C discharge at 25 °C	0.2102	0.0794	0.2153
LFP battery 0.5 C charge 1 C discharge at 15 °C	0.2805	0.3821	0.4416

[a] The R_{int} model here does not embed prior information about aging.

Table A.2
Training epochs for different electrical models embedded in BINN.

Condition	R_{int} [a]	Thevenin	PNGV
LFP battery 0.5 C charge 2 C discharge at 35 °C	356	698	599
LFP battery 0.5 C charge 3 C discharge at 25 °C	368	736	531
LFP battery 0.5 C charge 1 C discharge at 15 °C	317	798	596

[a] The R_{int} model here does not embed prior information about aging.
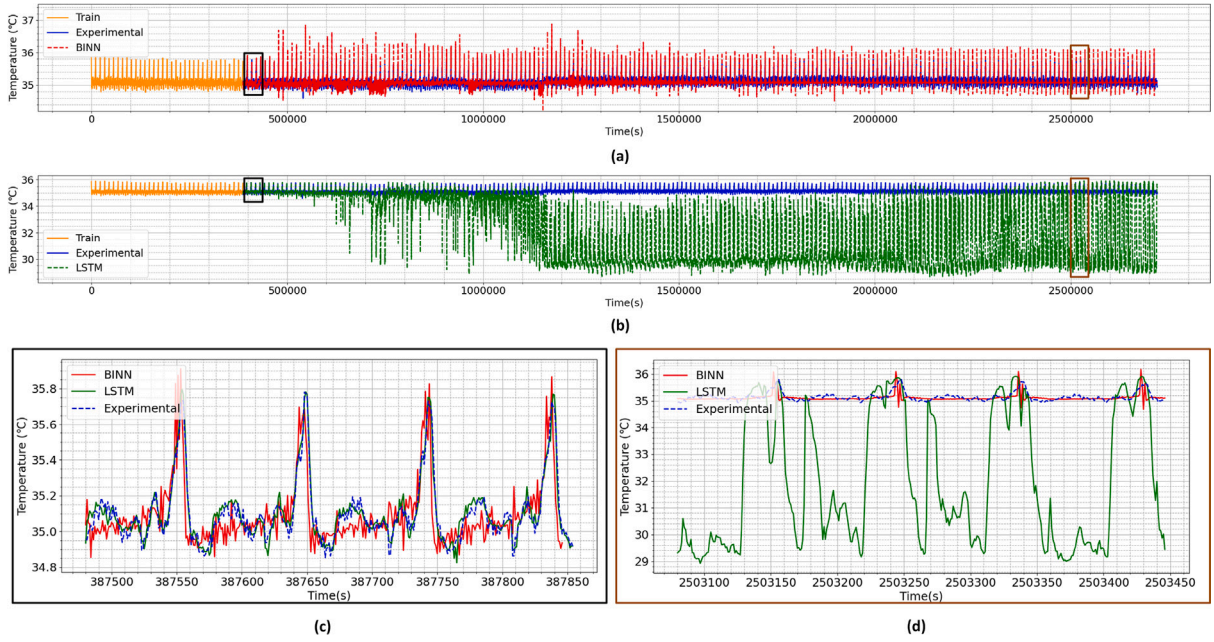
Fig. 8. Few data under 0.5 C charging and 1 C discharging condition at the ambient temperature of 35 °C are used as the training data. (a) (b) shows the prediction of BINN and LSTM in the latter cycle. (c) is the prediction of several cycles of BINN and LSTM following the training data. (d) is the prediction of BINN and LSTM after the lithium battery runs for 200 cycles.
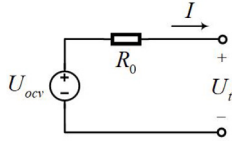

Fig. A.1. The circuit used in the R_{int} model.
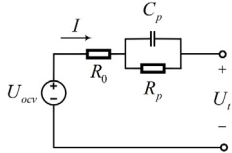

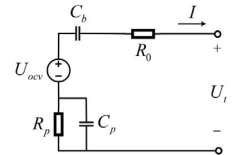**Fig. A.2.** The circuit used in the Thevenin model.

Fig. A.3. The circuit used in the PNGV model.

storage capacitance which reflects the accumulation of current, U_b is the voltage on C_b (see Tables A.1 and A.2).

$$U_t = U_{ocv} - I * R_0 - U_p - U_b$$

$$\frac{dU_p}{dt} = -\frac{U_p}{R_p C_p} + \frac{I}{C_p} \qquad (A.3)$$

$$\frac{dU_b}{dt} = \frac{I}{C_b}$$

References

[1] M. Li, J. Lu, Z. Chen, K. Amine, 30 years of lithium-ion batteries, Adv. Mater. 30

(33) (2018) 1800561, http://dx.doi.org/10.1002/adma.201800561, arXiv:https://onlinelibrary.wiley.com/doi/pdf/10.1002/adma.201800561.

[2] X. Zhang, Z. Li, L. Luo, Y. Fan, Z. Du, A review on thermal management of lithium-ion batteries for electric vehicles, Energy 238 (2022) 121652, http://dx.doi.org/10.1016/j.energy.2021.121652.

[3] G. Xia, L. Cao, G. Bi, A review on battery thermal management in electric vehicle application, J. Power Sources 367 (2017) 90–105, http://dx.doi.org/10.1016/j.jpowsour.2017.09.046.

[4] Y. Liu, J. Zhang, Self-adapting J-type air-based battery thermal management system via model predictive control, Appl. Energy 263 (2020) 114640, http://dx.doi.org/10.1016/j.apenergy.2020.114640.

[5] S. Dey, H.E. Perez, S.J. Moura, Model-based battery thermal fault diagnostics: Algorithms, analysis, and experiments, IEEE Trans. Control Syst. Technol. 27 (2) (2019) 576–587, http://dx.doi.org/10.1109/TCST.2017.2776218.

[6] I. Oyewole, A. Chehade, Y. Kim, A controllable deep transfer learning network with multiple domain adaptation for battery state-of-charge estimation, Appl. Energy 312 (2022) 118726, http://dx.doi.org/10.1016/j.apenergy.2022.118726.

[7] S. Song, C. Fei, H. Xia, Lithium-ion battery SOH estimation based on XGBoost algorithm with accuracy correction, Energies 13 (4) (2020) http://dx.doi.org/10.3390/en13040812.

[8] J. Tian, R. Xiong, W. Shen, State-of-health estimation based on differential temperature for lithium ion batteries, IEEE Trans. Power Electron. 35 (10) (2020) 10363–10373, http://dx.doi.org/10.1109/TPEL.2020.2978493.

[9] X. Du, Q. Wu, Y.-N. Wang, T.-S. Pan, Y.-M. Wei, H.-S. Chen, W.-L. Song, D.-N. Fang, Visualizing two-dimensional internal temperature distribution in cylindrical Li-ion cells, J. Power Sources 446 (2020) 227343, http://dx.doi.org/10.1016/j.jpowsour.2019.227343.

[10] G.-H. Kim, A. Pesaran, R. Spotnitz, A three-dimensional thermal abuse model for lithium-ion cells, J. Power Sources 170 (2) (2007) 476–489, http://dx.doi.org/10.1016/j.jpowsour.2007.04.018.

[11] S. Chen, C. Wan, Y. Wang, Thermal analysis of lithium-ion batteries, J. Power Sources 140 (1) (2005) 111–124, http://dx.doi.org/10.1016/j.jpowsour.2004.05.064.

[12] J. Kleiner, L. Komsiyska, G. Elger, C. Endisch, Thermal modelling of a prismatic lithium-ion cell in a battery electric vehicle environment: Influences of the experimental validation setup, Energies 13 (1) (2020) http://dx.doi.org/10.3390/en13010062.

[13] B. Rieger, S.V. Erhard, S. Kosch, M. Venator, A. Rheinfeld, A. Jossen, Multi-dimensional modeling of the influence of cell design on temperature, displacement and stress inhomogeneity in large-format lithium-ion cells, J. Electrochem. Soc. 163 (14) (2016) A3099–A3110, http://dx.doi.org/10.1149/2.1051614jes.

[14] M. Farag, H. Sweity, M. Fleckenstein, S. Habibi, Combined electrochemical, heat generation, and thermal model for large prismatic lithium-ion batteries in real-time applications, J. Power Sources 360 (2017) 618–633, http://dx.doi.org/10.1016/j.jpowsour.2017.06.031.

[15] N. Damay, C. Forgez, M.-P. Bichat, G. Friedrich, Thermal modeling of large prismatic LiFePO4/graphite battery. Coupled thermal and heat generation models for characterization and simulation, J. Power Sources 283 (2015) 37–45, http://dx.doi.org/10.1016/j.jpowsour.2015.02.091.

[16] A. Mevawalla, S. Panchal, M.-K. Tran, M. Fowler, R. Fraser, One dimensional fast computational partial differential model for heat transfer in lithium-ion batteries, J. Energy Storage 37 (2021) 102471, http://dx.doi.org/10.1016/j.est.2021.102471.

[17] C. Forgez, D. Vinh Do, G. Friedrich, M. Morcrette, C. Delacourt, Thermal modeling of a cylindrical LiFePO4/graphite lithium-ion battery, J. Power Sources 195 (9) (2010) 2961–2968, http://dx.doi.org/10.1016/j.jpowsour.2009.10.105.

[18] X. Hu, F. Feng, K. Liu, L. Zhang, J. Xie, B. Liu, State estimation for advanced battery management: Key challenges and future trends, Renew. Sustain. Energy Rev. 114 (2019) 109334, http://dx.doi.org/10.1016/j.rser.2019.109334.

[19] D. Zhang, S. Dey, S.-X. Tang, R. Drummond, S.J. Moura, Battery internal temperature estimation via a semilinear thermal PDE model, Automatica 133 (2021) 109849, http://dx.doi.org/10.1016/j.automatica.2021.109849.

[20] S. Panchal, I. Dincer, M. Agelin-Chaab, R. Fraser, M. Fowler, Thermal modeling and validation of temperature distributions in a prismatic lithium-ion battery at different discharge rates and varying boundary conditions, Appl. Therm. Eng. 96 (2016) 190–199, http://dx.doi.org/10.1016/j.applthermaleng.2015.11.019.

[21] F. Jaliliantabar, R. Mamat, S. Kumarasamy, Prediction of lithium-ion battery temperature in different operating conditions equipped with passive battery thermal management system by artificial neural networks, Mater. Today: Proc. 48 (2022) 1796–1804, http://dx.doi.org/10.1016/j.matpr.2021.09.026, Innovative Manufacturing, Mechatronics & Materials Forum 2021.

[22] S. Hochreiter, J. Schmidhuber, Long short-term memory, Neural Comput. 9 (8) (1997) 1735–1780, http://dx.doi.org/10.1162/neco.1997.9.8.1735.

[23] S. Zhu, C. He, N. Zhao, J. Sha, Data-driven analysis on thermal effects and temperature changes of lithium-ion battery, J. Power Sources 482 (2021) 228983, http://dx.doi.org/10.1016/j.jpowsour.2020.228983.

[24] J. Kleiner, M. Stuckenberger, L. Komsiyska, C. Endisch, Real-time core temperature prediction of prismatic automotive lithium-ion battery cells based on artificial neural networks, J. Energy Storage 39 (2021) 102588, http://dx.doi.org/10.1016/j.est.2021.102588.

[25] M. Raissi, P. Perdikaris, G. Karniadakis, Physics-informed neural networks: A deep learning framework for solving forward and inverse problems involving nonlinear partial differential equations, J. Comput. Phys. 378 (2019) 686–707, http://dx.doi.org/10.1016/j.jcp.2018.10.045.

[26] Y. Chen, L. Lu, G.E. Karniadakis, L.D. Negro, Physics-informed neural networks for inverse problems in nano-optics and metamaterials, Opt. Express 28 (8) (2020) 11618–11633, http://dx.doi.org/10.1364/OE.384875.

[27] M. Raissi, A. Yazdani, G.E. Karniadakis, Hidden fluid mechanics: Learning velocity and pressure fields from flow visualizations, Science 367 (6481) (2020) 1026–1030, http://dx.doi.org/10.1126/science.aaw4741, arXiv:https://www.science.org/doi/pdf/10.1126/science.aaw4741.

[28] L. Lu, X. Meng, Z. Mao, G.E. Karniadakis, DeepXDE: A deep learning library for solving differential equations, SIAM Rev. 63 (1) (2021) 208–228, http://dx.doi.org/10.1137/19M1274067, arXiv:https://doi.org/10.1137/19M1274067.

[29] K.E. Thomas, J. Newman, Thermal modeling of porous insertion electrodes, J. Electrochem. Soc. 150 (2) (2003) A176, http://dx.doi.org/10.1149/1.1531194.

[30] F. Feng, S. Teng, K. Liu, J. Xie, Y. Xie, B. Liu, K. Li, Co-estimation of lithium-ion battery state of charge and state of temperature based on a hybrid electrochemical-thermal-neural-network model, J. Power Sources 455 (2020) 227935, http://dx.doi.org/10.1016/j.jpowsour.2020.227935.

[31] M. Schmid, U. Vögele, C. Endisch, A novel matrix-vector-based framework for modeling and simulation of electric vehicle battery packs, J. Energy Storage 32 (2020) 101736, http://dx.doi.org/10.1016/j.est.2020.101736.

[32] A. Vaswani, N. Shazeer, N. Parmar, J. Uszkoreit, L. Jones, A.N. Gomez, Ł. Kaiser, I. Polosukhin, Attention is all you need, in: I. Guyon, U.V. Luxburg, S. Bengio, H. Wallach, R. Fergus, S. Vishwanathan, R. Garnett (Eds.), Advances in Neural Information Processing Systems, Vol. 30, Curran Associates, Inc., 2017.

[33] K.A. Severson, P.M. Attia, N. Jin, N. Perkins, B. Jiang, Z. Yang, M.H. Chen, M. Aykol, P.K. Herring, D. Fraggedakis, M.Z. Bazant, S.J. Harris, W.C. Chueh, R.D. Braatz, Data-driven prediction of battery cycle life before capacity degradation, Nat. Energy 4 (5) (2019) 383–391.

[34] Y. Preger, H.M. Barkholtz, A. Fresquez, D.L. Campbell, B.W. Juba, J. Romàn-Kustas, S.R. Ferreira, B. Chalamala, Degradation of commercial lithium-ion cells as a function of chemistry and cycling conditions, J. Electrochem. Soc. 167 (12) (2020) 120532, http://dx.doi.org/10.1149/1945-7111/abae37.